Numerical modeling and experimental study of self-propagating flame fronts in Al/CuO thermite reactions

Emelian Tichtchenko, H. Magliano, T. Wu, Lea Pillemont, Olivier Simonin, B. Bédat, A. Estève, C. Rossi

Numerical Modeling and Experimental Study of Self-Propagating Flame Fronts in Al/CuO Thermite Reactions

E. Tichtchenko[a,b], H. Magliano[a,b], T. Wu[a], L. Pillemont[a,b], O. Simonin[b], B. Bédat[b], A. Estève[a], C. Rossi[a]

[a] *LAAS-CNRS, University of Toulouse, 7 Avenue du colonel Roche, Toulouse, 31400, France*
[b] *IMFT-CNRS, University of Toulouse, 2 allee du Pr Camille Soula, Toulouse, 31400, France*

Abstract

Nanothermites are promising energetic materials as their high-temperature reaction driven by the oxidation of a metallic fuel associated with the reduction of an oxidizer, can exhibit extremely fast burning rates, exceeding hundreds of m.s^{-1}. In addition, by modifying reactant size, stoichiometry and compaction conditions, reaction properties (temperature, intermediate reactions, by-products) and combustion rates can be tailored, making it possible to customize combustion properties for each application. Unfortunately, in spite of three decades of research in the field of thermites, there is no predictive physical models able to provide design guidelines to experimentalists. The reason of this is that the complex multiphasic physics governing thermite combustion, where combustion gases interact with burning particles, is still poorly understood and documented, while being the key step to depict the dynamics of the flame front. The purpose of this work is to propose a first one-dimensional (1D) model that describes the dynamics of the reaction front propagation in Al/CuO powdered thermite considering the reacting flow combined with heat transfer, chemistry and fluid flow. CuO was chosen as it is the widest used metallic oxidizer, that decomposes below the flame temperature, leading to a gas phase driven reaction. Separate mass, momentum and energy transport equations for the three phases, namely Al, CuO particles and gas mixture, are written in the frame of an Euler-Euler approach for multiphase reactive flows. These equations are coupled by modeled interphase transfer terms. The theoretical formulation and numerical methods are detailed. After validating the model with experimental case studies —specifically, the combustion of Al/CuO powder in open glass tubes— numerical experiments are performed to demonstrate the utility of the code in (i) analyzing the multiphase flow dynamics at the thermite flame front, and (ii) examining the critical powder characteristics that affect the burn rate.

Keywords: Combustion, Thermite, Flame dynamics, Multiphase flow

Nomenclature

Index

f	Flame
$g \rightarrow m$	Transfer from gas phase to phase m
g	Gas phase
i	Atomic species i
i,m	Atomic species i in phase m
liq	Liquid
m	One of the three phases p, q, or g
max	Maximum
min	Minimum
$p \rightarrow q$	Transfer from phase p to phase q
p	Al particulate phase
q	CuO particulate phase
s	Al and CuO particulate phases ($s = p + q$)

Greek Symbols

α	Volume fraction
Δu	Velocity difference
$\dot{\omega}^r$	Source term for mass production or loss (reactions)
ε	Emissivity
λ	Thermal conductivity
Π	Total heat transfer
ρ	Density
σ	Stefan-Boltzmann constant
φ	Stoichiometric ratio of Al to CuO

Latin Symbols

A	Specific surface area
C_d	Drag coefficient
D	Diffusion coefficient
d	Diameter of particles
e	Energy terms
I	Interphase momentum transfer term
k	Thermal conductivity
L_t	Length of the tube
n	Number of particles
Nu	Nusselt number
P	Pressure
P^{fric}	Frictional pressure component
P_s	Frictional pressure between particles
Pr	Prandtl number
q	Heat transfer
q^{cond}	Conductive heat transfer
q^{rad}	Radiative heat transfer
R	Universal gas constant
r_t	Radius of the tube
Re	Reynolds number
T	Temperature
u	Velocity
$u_{\sigma_{mg}}$	Velocity of gas crossing particulate phase m
V	Volume
W	Molar mass
Y	Mass fraction

1. Introduction

Mixtures of Al/metal-oxide particles of sizes in the range 10^2 – 10^3 nm, commonly known as nanothermites, can burn in a self-sustained reaction with an ultra-high energy density. One of the most attractive aspects of nanothermites is the tunability in terms of burn rate and pressure development, making them good candidates for a variety of civilian and defense applications [1, 2, 3, 4, 5, 6, 7]. Typically, the burn rate can be tuned in the ranges of 10^{-1} – 10^3 m.s^{-1} and the peak pressure in constant volume cell spans a few to tens of MPa varying the reactant composition and size, reactant intimacy and the stoichiometry. Accurately predicting combustion characteristics, such as the propagation front velocity and flame width, based on parameters like particle size of aluminum and oxides, compaction, stoichiometry, and environmental conditions, remains a significant challenge in designing nanothermite materials optimized for specific applications. Current thermite combustion models [8, 9, 10, 11, 12, 13] suffer from over-simplifications which severely limit their ability to establish such structure-property relationships. For example, in [8], a simplified gasless analytical approach was proposed to model the thermal front propagation in Al/MoO_3 nanothermite, presuming homogeneous combustion waves and a single-step reaction mechanism described by an Arrhenius equation, with the degree of reaction varying linearly from one to zero across the reaction zone. It also assumes constant thermophysical properties which limits its predictive capability. Subsequently, de Lemos et al. [11, 12, 13] developed an equivalent gasless combustion approach to simulate thermal front propagation in Al/Fe_2O_3 nanothermites, aimed at applications in thermal plugging and abandonment processes. Similar to the model in [8], the exothermic thermite reaction is represented as a single-step reaction through a source term in the energy equation, which does not fully capture the complexity of the actual reaction mechanisms. Furthermore, all these gasless approaches rely on empirically determined activation energies and prefactors obtained through calibration, and do not incorporate critical factors, such as reactant particle size and powder density, as input parameters in the reaction term. These factors, however, have a significant impact on the reaction rate and should not be overlooked. Epps et al. in [14] introduced an interesting approach to account for the advection of gas contained in a porous thermite matrix via Darcy's law. But again, the thermite reaction is reduced to a single Arrhenius law with a rough estimate of the gas released limiting the applicability of such approach. No model currently exists for accurately describing heterogeneous flame propagation during thermite reactions.

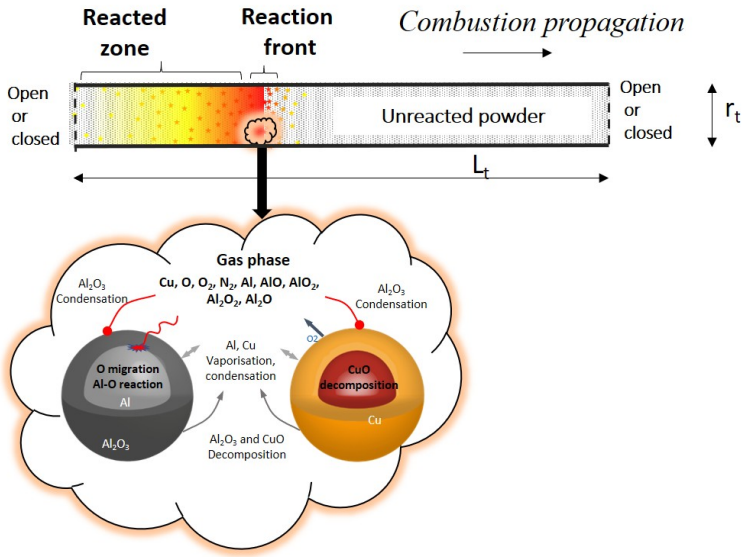

Figure 1: Schematic of the modeled system : a semi-infinite cylindrical tube filled with Al/CuO powdered thermite. Zoom-in : detailed schematic illustrating mass transfer and chemical reactions.

This study proposes to model the multiphase, multispecies, self-propagating combustion process in Al/CuO thermites within a cylindrical tube. The proposed approach enables the accurate description of the temperature and pressure profiles ($T(x,t)$, $P(x,t)$) in each phase (gas and particles), the tracking of gas- and condensed-phase species in the reaction front, and, as key metrics, and, the prediction of key metrics, such as flame velocity (u_f). An Euler-Euler approach is employed to model the interaction between the two reactive particulate phases, aluminum, p, and CuO, q, and the gaseous phase, g, involving 9 reactive species (Al, Cu, O_2, N_2, Al_2O, Al_2O_2, AlO, AlO_2, O). It involves solving the mass, momentum, and energy transport equations in the three separate phases. Additional equations of species mass fraction are employed to model the evolution of gaseous and particulate phases composition. And, the different phases are coupled through specific closure laws that describes the interphase mass, momentum, and energy transfers. In addition, the model integrates an ensemble of chemical reactions, and physical transformations that are known to occur in the gas phase during the thermite reaction. This represents the most advanced thermite combustion model, providing a detailed and precise description of combustion dynamics for variable thermite powder configurations in terms of particle size, stoichiometry, powder density, and other important parameters. This article is organized as follows. After the description of the physical system and considered chemical reactions in section 2, the continuous model is presented in detail in Section 3. Section 4 provides simulation details and presents the numerical methods as well as experimental procedures used to compare theoretical predictions with combustion tests. Finally, through 3 experimental case-studies, numerical experiments are presented in section 5, illustrating the interest of the model to analyze the multiphase flow physics at the thermite flame front, and, predict the flame front propagation as a function of powder characteristics.

2. Description of the system

The system is a cylindrical tube filled with an homogeneous mixture of Al and CuO particles in air. The tube (Fig. 1, radius r_t and length L_t) is isotropic according to the lateral dimensions. r_t and L_t are input parameters. The combustion front propagates to the right, along the x axis, at the rate u_f. The left and right boundary conditions can be opened, fully-closed or partially opened. The initial Al particle purity (Y_{Al}), the powder compaction (α_s), the particles' diameter (d_p and d_q, for Al and CuO particle respectively), and stoichiometric ratio (Al over CuO ratio, φ) are the main input parameters defining the initial thermite. To initiate the Al/CuO reaction, an input energy of 600 kJ.kg^{-1} is injected uniformly at the left side of the tube. During the combustion, we consider three phases, noted p, q and g, for the Al particulate phase, CuO particulate phase, and the gas phase, respectively. The main heterogeneous

reactions and phase transitions involved between the particulate and the gas phases are: (1) oxidation of aluminum by oxygen species (O_2 and O); (2) decomposition of CuO releasing oxygen species in the gas phase; (3) decomposition of the alumina shell, which generates molecular oxygen and atomic aluminum; (4) vaporization/condensation of atomic Al and Cu; for the sake of simplicity, they are treated similarly to heterogeneous reactions, based on the gas/liquid equilibrium. In the gas phase, in addition to Al, Cu, O_2, O, we include 4 Al suboxides species - Al_2O, Al_2O_2, AlO, AlO_2 - as well as N_2. The gas-phase kinetics are modeled based on the scheme proposed by Bucher et al. [15, 16]. The open-source tool Cantera dedicated to rate theory calculations was used to solve the set of differential equations associated with the gas phase reactions. Details can be found in [17] and a summary of the reactions in both particulate and gas phases is given in Table 1 and 2.

Table 1: Gas phase chemical reactions with associated kinetic parameters, defined as $AT^n e^{-B/T}$. X corresponds to the gas phase species Al, Cu, O, O_2, Al_2O, AlO, Al_2O_2, AlO_2, N_2.

Chemical reaction	**A** ($cm^3 mol^{-1} s^{-1}$)	**B** (K)	**n**
$Al + O_2 \leftrightarrow AlO + O$	9.7×10^{13}	80.5	0
$AlO + O_2 \leftrightarrow AlO_2 + O$	4.6×10^{14}	10008	0
$Al_2O_2 \leftrightarrow AlO + AlO$	1.0×10^{15}	59335	0
$Al_2O_2 \leftrightarrow Al + AlO_2$	1.0×10^{15}	74937	0
$Al_2O_2 \leftrightarrow Al_2O + O$	1.0×10^{15}	52466	0
$Al + O_2 \leftrightarrow AlO + O$	1.0×10^{15}	44564	0
$Al + O_2 \leftrightarrow AlO + Al$	1.0×10^{15}	67035	0
$Al + O + X \leftrightarrow AlO + X$	3.0×10^{17}	0	-1
$O_2 + X \leftrightarrow O + O + X$	1.2×10^{14}	54244	0

Table 2: Heterogeneous chemical reactions. (g) and (c) stand for gas and condensed phases respectively. Note that condensed phases can exist as either solid or liquid, depending on their temperature.

Reaction	**Mechanism**	**Mathematical Implementation**
$2Al_{(c)} + 3/2O_{2(g)} \rightarrow Al_2O_{3(c)}$	Diffusion-Reaction	Spalding/spontaneous reaction
$2Al_{(c)} + 3O_{(g)} \rightarrow Al_2O_{3(c)}$	Diffusion-Reaction	Spalding/spontaneous reaction
$Al_2O_{3(c)} \rightarrow 2Al_{(g)} + 3/2O_{2(g)}$	Decomposition	Arrhenius
$CuO_{(c)} \rightarrow Cu_{(c)} + 1/2O_{2(g)}$	Decomposition	Arrhenius
$Cu_{(c)} \leftrightarrow Cu_{(g)}$	Evaporation-Condensation	Spalding/Clapeyron
$Al_{(c)} \leftrightarrow Al_{(g)}$	Evaporation-Condensation	Spalding/Clapeyron
$Al_xO_{y(g)}$	Condensation	Spalding/spontaneous reaction

3. Physical Model

An Euler-Euler approach similar to that used in [18, 19] is employed to model the interaction between the reactive particulate phases (solid or liquid, depending on their temperature) and the gas mixture. This method builds upon a continuous model originally developed by Lanthouwers et al. [20] to describe the thermofluid dynamics of dense reactive gas-solid mixtures, which has been simplified for our 1D case. It involves solving the mass, momentum, and energy transport equations in the three separate phases. Additional equations of species mass fraction are employed to model the evolution of gaseous and particulate phases composition. A last set of equations are used to predict the average diameter of each particulate phase. Also, the different phases are coupled through specific closure models that account for interphase mass, momentum, and energy transfers.

3.1. Mass, momentum and energy transport equations

This section presents the system of equations governing the evolution of mass, momentum, and energy for each phase. Since the particulate phases p and q follow the same mathematical model, the equations are presented for phase p only.

3.1.1. Mass

$$\partial_t(\rho_m \alpha_m) = -\partial_x(\rho_m \alpha_m u_m) + \Gamma_m \tag{1}$$

where ρ_m, α_m, u_m are respectively the density, the volume fraction and the velocity of the phase m with $m = p, q, g$. Γ_m represents the interphase mass transfer rate per unit volume [17, 21], which satisfies the condition $\Gamma_g + \Gamma_p = 0$. Note that Equation 1 is applied to calculate the volume fractions of both particulate phases, but not the volume fraction of the gas phase which is instead determined from the condition : $\sum_m \alpha_m = 1$.

3.1.2. Momentum

The particulate phase p momentum transport equation is written as:

$$\partial_t(\rho_p \alpha_p u_p) = -\partial_x(\rho_p \alpha_p u_p u_p) - \partial_x(\alpha_p P_p) + I_{g\to p} + I_{q\to p} + \Gamma_{g\to p} u_{\sigma_{pg}} \tag{2}$$

P_p is the pressure in the solid phase p detailed in section 3.4.2. $I_{q\to p}$ and $I_{g\to p}$ represent the interphase momentum transfers respectively, from the solid phases q to p and from the gas to phase p, due to particle-particle collisions and frictional effects. The term $\Gamma_{g\to p} u_{\sigma_{pg}}$ accounts for the momentum transfer associated with the interphase (gas-particle) mass transfer (corresponding to Γ_m in Equation 1). $u_{\sigma_{pg}}$ is the mean velocity of the mass flux crossing the particle p surfaces. The relation between $I_{g\to p}$ and $I_{m\to g(m=p,q)}$, given by Equations 23 and 24, is detailed in section 3.4.3. It is important to note that gravitational forces are not considered in this model, as the system is oriented horizontally ($\alpha_p \rho_p g$ is neglected).

The momentum transport equation in the gas phase is given by:

$$\partial_t(\rho_g \alpha_g u_g) = -\partial_x(\alpha_g \rho_g u_g u_g) - \partial_x(\alpha_g P_g) + \sum_{m=p,q} I_{m\to g} + \sum_{m=p,q} \Gamma_{m\to g} u_{\sigma_{mg}} \tag{3}$$

$I_{m\to g}$, which represents the momentum transfers between the two solid phases and the gas, is detailed in section 3.4.3. As for particulate phases, the term $\Gamma_{m\to g} u_{\sigma_{mg}}$ accounts for the momentum transfer associated with the interphases (particles - gas) mass transfer.

3.1.3. Energy

The specific internal energy of particulate phase p, denoted as e_p, is defined as : $\sum_i Y_{i,p} e_{i,p}(T_p)$ where $e_{i,p}(T_p)$ is the total internal specific energy of the species i at the temperature T_p considering the formation and sensible energy. $Y_{i,p}$ is the volume fraction of species i in particulate phase p. $e_{i,p}(T_p)$ considering the variation of both the heat capacity and phase change (liquid/solid) of species i is calculated as:

$$e_{i,p}(T_p) = \begin{cases} e_{i,p(s)}(T_p) & T_p < T_{liq,i} \\ e_{i,p(l)}(T_p) & T_p > T_{liq,i} \end{cases} \tag{4}$$

The gaseous specific energy is calculated as : $e_g = 0.5\|u_g\|^2 + \sum_i Y_{i,g} e_{i,g}(T_g)$, where $e_{i,g}(T_g)$ represents the total internal specific energy of species i at temperature T_g, including both formation and sensible energy. $Y_{i,g}$ is the mass fraction of the species i in the gas phase.

Both $e_{i,p(s)}(T_p)$ and $e_{i,p(l)}(T_p)$ are computed based on NIST polynomials [22]. And, the values for $e_{i,g}(T_g)$ are calculated using the NASA7 polynomials.

In the particulate phase, the conservation energy equation is written as:

$$\partial_t(\rho_p \alpha_p e_p) = -\partial_x(\rho_p \alpha_p u_p e_p) + \partial_x q^{rad} + \partial_x q^{cond} + \Pi_p \tag{5}$$

$\partial_x q^{rad}$, $\partial_x q^{cond}$ are respectively the radiative and conductive heat flux in the considered particulate phase and $\Pi_p = \sum_{m\neq p} \Pi_{m\to p}$ denotes the total heat transfer from phases $m = g, q$ to p. In the x axis, the interactions between particles are accounted for in the friction term (section 3.4.2). It is important to note that, because the model is unidirectional, the perpendicular axes are not resolved, and thus it does not account for any lateral heat losses through the tube wall.

In the gas phase, the conservation energy equation is written as:

$$\partial_t(\rho_g \alpha_g e_g) = -\partial_x(\rho_g \alpha_g u_g e_g) - \partial_x(\alpha_g P_g u_g) + \sum_{m=p,q} 0.5\Gamma_{m\to g} u^2_{\sigma_{mg}} + q_g \tag{6}$$

$q_g = q_{g\to g} + q_{p\to g} + q_{q\to g}$ is the radiative and conductive heat transfers. The term $\sum_{m=p,q} 0.5\Gamma_{m\to g} u^2_{\sigma_{mg}}$ represents the kinetic energy associate to mass tranfer between phases $m = p,q$ to the gas phase (Γ_m in Equation 1).

3.2. Evolution of the particle composition

$$\partial_t(\rho_p \alpha_p Y_{i,p}) = -\partial_x(\rho_p \alpha_p u_p Y_{i,p}) + \partial_x D_{i,p} \partial_x Y_{i,p} + \sum_{r\in R} \dot{\omega}^r_{i,g(p)} \tag{7}$$

where $D_{i,p}$ is the diffusion coefficients of specie i in particle p, considered null in this model. $\dot{\omega}^r_{i,g(p)}$ are source terms representing the species vanishing or production due to gas-solid mass transfer mechanisms, i.e. condensation, vaporization or migration (Table 2). The density ρ_p is computed assuming the density of any species i constant :

$$\rho_p = \left(\sum_i \frac{Y_{i,p}}{\rho_{i,p}} \right)^{-1} \tag{8}$$

3.3. Evolution of the gas mixture properties

The evolution of the gas mixture properties is predicted using the 9 transport equations (one per gaseous species, i) written as follows :

$$\partial_t(\rho_g \alpha_g Y_{i,g}) = -\partial_x(\rho_m \alpha_m u_m Y_{i,m}) + \partial_x D_{i,g} \partial_x Y_{i,g} + \sum_{r\in R} \dot{\omega}^r_{i,g(m)} \tag{9}$$

$\dot{\omega}^r_{i,g(m)}$ are source terms representing the species disappearance or production due to chemical reactions listed in Table 1. The density of the gaseous mixture ρ_g is calculated based on the ideal gas law assumption.

$$\rho_g = \left(\sum_i \frac{Y_{i,g}}{W_i} \right)^{-1} \frac{P_g}{RT_g},$$

where W_i represents the molar mass of species i. T_g and R are the gas temperature and universal gas constant, respectively.

3.4. Interphase coupling modelling

The effects of the interphase interactions are taken into account in the conservation Equations 1, 2 and 3 through the presence of particle-to-gas and gas-to-particle mass and momentum transfer terms which are detailed thereafter.

3.4.1. Interphase mass transfer

According to the chemical reactions in both gas and particulate phase the mass transfer rates, Γ_m with $m = p,q,g$ are calculated as :

$$\begin{aligned} \Gamma_g &= \sum_{m=p,q} \Gamma_{m\to g} = \sum_{m=p,q} \sum_{r\in R} \sum_i \dot{\omega}^r_{i,g(m)} \\ \Gamma_p &= \Gamma_{g\to p} = -\Gamma_{p\to g} = -\sum_{r\in R} \sum_i \dot{\omega}^r_{i,g(p)} \end{aligned} \tag{10}$$

where r represents one reaction from the set of reactions R which are summarized in Tables 1 and 2. $\dot{\omega}^r_{i,g(m)}$ refers to the gaseous source term for species i associated with reaction r occurring in the particulate phase m. Additionally, $\dot{\omega}^r_{i,g(p)}$ denotes the overall gaseous source term for species i corresponding to reaction r.

3.4.2. Solid-solid interactions

The solid-solid interactions can be classified into three primary contributions: friction, collisions and kinetics. However, in this study, we disregard the kinetics factors since particle agitation is neglected because our model is conducted along a single axis (1D).

Frictional transfer. The particulate phase pressure, P_p represents the internal pressure within phase p arising from the friction among the solid particles themselves, as well as from their interactions with the surrounding fluid. It can be written as :

$$P_p = P^{fric_{p\to p}} + P^{fric_{p\to q}} \tag{11}$$

where $P^{fric_{p\to p}} = \frac{\alpha_p^2}{\alpha_s^2} P_s$, and, $P^{fric_{p\to q}} = \frac{\alpha_p \alpha_q}{\alpha_s^2} P_s$. α_s represents the total particulate phase volume fraction, i.e. $\alpha_p + \alpha_q$. P_s is the frictional pressure of the two particulate phases as defined by Johnson & Jackson [23] in monodisperse mixture :

$$P_s = F_0 \frac{(\alpha_s - \alpha_{s,min})^r}{(\alpha_{s,max} - \alpha_s)^s} \tag{12}$$

We assume $\alpha_{s,max} = 0.64$ as the maximum volume fraction and set $\alpha_{s,min} = 0.5$ as the lower threshold to trigger collisional pressure. r, s and F_0 are emperical parameters equal to 2, 5 and 0.05, respectively. Finally, P_p is written as :

$$P_p = \frac{\alpha_p}{\alpha_s} P_s \tag{13}$$

Collisional contribution. The collisions are approximated by assuming $\Delta u_{qp} = u_q - u_p$ as:

$$I_{q\to p} = \mu_p P^{fric_{p\to q}} \frac{\Delta u_{qp}}{\|\Delta u_{qp}\|} = \mu_p \frac{\alpha_p \alpha_q}{\alpha_s^2} P_s \frac{\Delta u_{qp}}{\|\Delta u_{qp}\|} \tag{14}$$

We took $\mu_p = 0.4$

3.4.3. Gas-particle interactions

The gas to particulate phase momentum transfer due to drag forces can be written as:

$$I_{g\to p} = n_p < F_{g\to p} > \tag{15}$$

where n_p is the particle number of phase p, which is calculated as : $n_p = \alpha_p / < V_p >$ where $< V_p >$ represents the averaged particle volume. $< F_{g\to p} >$ is the force exerted by the gas on one particle. According to [24], these forces are approximated as the sum of the Archimedes force, $< V_p > \partial_x P_g$, and, the drag force, $< F^d_{g\to p} >$ that can be modelled by Equation 17, considering $\Delta u_{gp} = u_g - u_p$.

Finally,

$$I_{g\to p} = n_p(< F^d_{g\to p} > - < V_p > \partial_x P_g) \tag{16}$$

$$< F^d_{g\to p} > = m_p \tau_p^{-1} \Delta u_{gp} \tag{17}$$

where m_p is the particulate phase mass, and τ_p is calculated from :

$$\tau_p^{-1} = \frac{3}{4} \frac{\rho_g}{\rho_p} \frac{\|\Delta u_{gp}\|}{d_p} C_d \tag{18}$$

where d_p is the p particle diameter and C_d is the drag coefficient, defined as the minimum value between the *Wen & Yu* formulation [25] and the Ergun one. [26].

$$C_d = \begin{cases} C_{d,WY} & \alpha_g > 0.7 \\ \min(C_{d,WY}, C_{d,Er}) & \text{Otherwise} \end{cases} \tag{19}$$

With :

$$C_{d,WY} = \begin{cases} \frac{24}{Re_s}\left[1+0.15Re_s^{0.687}\right]\alpha_g^{-1.7} & Re_s < 1000 \\ 0.44\alpha_g^{-1.7} & \text{Otherwise} \end{cases} \tag{20}$$

and :

$$C_{d,Er} = 200\frac{\alpha_s}{Re_s} + \frac{7}{3} \tag{21}$$

Re_s, the solid-phase Reynolds number, is defined as :

$$Re_s = \alpha_g \frac{\rho_g \|\Delta u_{gp}\| d_p}{\mu_g} \tag{22}$$

Finally, $I_{g\to p}$ is written as :

$$I_{g\to p} = -\alpha_p \partial_x P_g + \alpha_p \rho_p \tau_p^{-1} \Delta u_{gp} \tag{23}$$

The momentum transfer from the particulate phase to the gas due to drag forces, $I_{p\to g}$, is calculated using Equation:

$$\sum_{m=p,q} I_{m\to g} + I_{g\to m} = -\partial_x \alpha_s P_g = -\partial_x P_g + \partial_x(\alpha_g P_g) \tag{24}$$

3.5. Interphase heat transport models

The Π_p term in Equation 5 contains conductive and radiative heat transfer term between the two particulate phases. The contribution of heat transfer by conduction between the gas and particulate phases is calculated using a spherically integrated form of Fourier's law :

$$q_{g\to p,q}^{cond} = -\lambda_g \pi Nu[d_p(T_p - T_g)n_p + d_q(T_q - T_g)n_q] \tag{25}$$

where the Nusselt number is defined as follows [27] : $Nu = (7 - 10\alpha_g + 5\alpha_g^2)(1 + 0.7Re_{p \text{ or } q}^{0.2} Pr^{1/3})$. Finally, we also account for the heat transfer related to the mass transfer (for each species i) which is described in [17].
The heat transfer conduction and radiation terms for each phase $m = g, p, q$ are modeled based on Zehner & Bauer formulation [28] using a unit cell approach, where the total gas conductivity normalized to the particulate phases (Al+CuO) conductivity $k_s = \lambda_s/\lambda_g$ is defined as:

$$k_s = \underbrace{\left(1 - \sqrt{1-\alpha_g}\right)\alpha_g\left[(\alpha_g - 1 + k_G^{-1})^{-1} + k_{rad}\right]}_{k'_g} + \underbrace{\sqrt{1-\alpha_g}[\varphi k_s + (1-\varphi)k_c]}_{k'_s} \tag{26}$$

k'_g is the effective normalized bulk gas conductivty, while k'_s is the effective normalized conductivity of the unit cell core, that include the particle phase conductivity and the interstitial gas one. k_G, k_{rad}, φ, k_c, k_s are respectively the contribution of Smoluchowski effect, radiation, particle flattening and the normalized core bulk conductivity, and the normalized volume arithmetic averaged conduction of the particles:

$$k_s = \frac{\lambda_s}{\lambda_g} = \frac{\sum_{m=p,q}\lambda_m n_m}{\lambda_g \sum_{m=p,q} n_m} \tag{27}$$

As Smoluchowski effect is neglected and the particles are assumed to be perfectly spherical, k_G and φ are set to 1 and 0 respectively. The effective normalized bulk gas conductivity k'_g and the effective normalized conductivity of the core of the unit cell k'_s are assumed to be the effective normalized conductivity of the gaseous phase and the sum of both normalized effective conductivities of particulate phase, respectively. The Zehner & Bauer formulation considers a mono-dispersed particulate phase. To adapt it to the bi-dispersed media, a volume weighted distribution of the heat flux going through the core of the unit cell is assumed between both particle phases p and q, such as the effective

normalized conductivity of the phase p is: $k'_p = (\alpha_p k'_s)/(\sum_{m=p,q} \alpha_m)$.

The calculation of the radiative heat flux between the two particulate phases ($q^{rad}_{p\to q}$) assumes a geometrically self-contained system, following Equation (28) [29], where σ, $A_p = 0.25 n_p \pi d_p^2$, and $F_{p\to q}$ represent the Stefan-Boltzmann constant, the total surface area of particulate phase p per unit volume, and the view factor, respectively. The view factor is estimated using Equation (29) as the ratio of the surface area of phase q to the sum of the particulate surface areas. While the emissivities of the particles, ε_p and ε_q, depend on temperature and composition, they are assumed constant and set to 0.85, which corresponds to the typical range of emissivities for metal oxides.

$$q^{rad}_{p\to q} = \frac{\sigma(T_p^4 - T_q^4)}{\frac{1-\varepsilon_p}{A_p\varepsilon_p} + \frac{1}{A_p F_{p\to q}} + \frac{1-\varepsilon_q}{A_q\varepsilon_q}} \tag{28}$$

$$F_{p\to q} = \frac{n_q d_q^2}{n_q d_q^2 + n_p d_p^2} \tag{29}$$

In the special case where both particulate phases behave as black bodies ($\varepsilon_p = \varepsilon_q = 1$), Equation (28) simplifies to:

$$q^{rad}_{p\to q} = \sigma(T_p^4 - T_q^4)\frac{1}{\frac{1}{n_q d_q^2} + \frac{1}{n_p d_p^2}} \tag{30}$$

3.6. Particle number conservation equation

In addition to the mass, momentum and energy conservation, we consider no agglomeration or break-up of particles. Therefore, the number of particles in each phase p or q is conserved. From [30], the particle number conservation equation can be written as:

$$\partial_t(\rho_p \alpha_p \chi_p) = -\partial_x(\rho_p \alpha_p u_p \chi_p) \tag{31}$$

where $\chi_p = < m_p^{-1} >$. All the geometric quantities relative to the particles p such as d_p, V_p, S_p, etc. are computed based on χ_p and ρ_p by assuming that $\pi d_p^3 = 1/\rho_p \chi_p$ and $V_p = 1/6\pi d_p^3$ and $S_p = \pi d_p^2$. It has to be noted that there is no dispersion term as the particle agitation is neglected.

4. Simulation details and Experimental testbed

4.1. Thermophysical and kinetic parameters

All thermodynamical data, for particulate phases (being liquid or solid depending on their temperature) and gaseous species, come from NIST-JANAF tables [31]. The gas transport properties are computed based on the Lennard-Jones potential using Cantera [32] considering parameters found in the literature [33, 34]. The vaporization points of the aluminum metal and copper metal evolves with respect to the pressure follow a Clapeyron law. The three (k_0, E_a) couples characterizing the kinetics of CuO decomposition, Al_2O_3 decomposition and O species diffusion via an Arrhenius law are (5.97×10^5 kg.m^{-3}s^{-1}, 110×10^3 J.mol^{-1}K^{-1}), (1.52×10^6 kg.m^{-3}s^{-1}, 400×10^3 J.mol^{-1}K^{-1}) and (5.7×10^{-9} kg.m^{-3}s^{-1}, 110×10^3 J.mol^{-1}K^{-1}), respectively. These values were derived from [35, 36, 37].

4.2. Initial and boundary conditions

In the present work we simulate two sets of experiments, representing respectively semi-open and fully-closed burn tube. Open boundary means that the gas pressure (P_g) is set to 0.1 MPa and particle phase velocity is supposed constant at the boundary ($\partial_t u_p$=0). Closed boundary imposes the gas and particle phases velocity equal to 0 (u_g=u_q=u_q=0). Although, considering semi-infinite tube ($L_t >>$ flame front width), the right boundary of the tube has no effect on the propagating front dynamics, it is maintained open.

4.3. Numerical methods or computational scheme

The numerical resolution of the set of conservation equations described above are implemented under a vectorized form, which facilitates the use of a finite volume method.

$$\int_V \frac{\partial Q_m}{\partial t} dV = \int_A (F_m + D_m) dA + \int_V S_m dV \tag{32}$$

$$\begin{cases} Q_m = \alpha_m \rho_m q_m \\ q_m = \begin{bmatrix} 1 \\ u_m \\ e_m \\ Y_{m,i} \\ \chi_m \end{bmatrix} \end{cases} \tag{33}$$

where m represent the different phases. F_m includes advected terms and pressure terms relative to momentum equations solved using an AUSM+up numerical scheme [38]. D_m contains both the thermal transport terms (by conduction and radiation) and mass transport terms (species diffusion) evaluated via the divergence theorem. S_m represents interphase exchanges, in which volumetric terms are directly integrated in the volume. The one dimensional system is homogeneously discretized using Δx = 2 µm. And the time step for integrating all terms is dynamically varying during the simulation, according to a set of constraints, *i.e.*, mass fraction of species gradients, conduction, frictional pressure. A CFL stability conditions (0.09 for the gas and 0.3 for the particulate phases) are introduced.

4.4. Thermite samples prepared for model validation

The thermite mixture for each combustion test was formulated individually by combining Al and CuO in nano and/or micro scale. The nano aluminium (nAl, 80 nm with 68% active content) and micro aluminium (µAl, 0.8 µm with 65% active content) were purchased from Novacentrix (Texas, USA). A second batch of micro aluminum (5 µm with 41% active content; 10 µm with 17% active content) was purchased from US Research Nanomaterials Inc. (Texas, USA). The active content of each aluminium was obtained by Thermogravimetric analysis under air. The nano CuO (<50 nm, purity $\geq$ 96%) and micro CuO (<10 µm, purity $\geq$ 98%) powder were purchased from Sigma Aldrich (France). Mixtures of different thermite materials were prepared using a classic sonication method where aluminum particles are mixed with CuO, respectively with an equivalence ratio of 1.2 in hexane followed by a 60 minutes sonication. The thermite powder was then collected and stored under N_2 after being dried in an oven at 45 °C for 24 hours.

Table 3: Characteristics of thermites used in the quartz tube burner for combustion tests

Thermite sample	**Mass (*mg*) of :**		**Total (*mg*)**	**density ($g.cm^{-3}$)**	**TMD%**
	Fuel	*Oxidizer*			
nAl/CuO	115	285	400	0.57	12
1-µAl/CuO	264	631	895	1.04	22
5-µAl/CuO	335	515	850	1.24	27
10-µAl/CuO	608	382	990	1.29	29

4.5. Experimental set up and procedure

Figure 2 shows the experimental setup. The tube used in the experiments has the internal radius equal to 2.5 mm with a wall thickness of 1.5 mm and total length of 10 cm. The thermite is filled inside the tube up to 3 – 4 cm length. The mass and packing density values, along with the burn rate, are provided in Table 3. The combustion is initiated by an igniter containing a 3 mg of energetic ink (Al/CuO/10% PVDF; PVDF: polyvinylidene fluoride) as described in [39]. The igniter is positioned on the left side of the quartz tube, and ignition is achieved by applying a DC current pulse with a constant power dissipation of 6 mJ. The igniter ignites at $\sim$ 0.02 ms, the flame generated by the igniter (Figure S1, Supplementary File) reaches the thermite filled inside the quartz tube at $\sim$ 0.04 ms. A high-speed

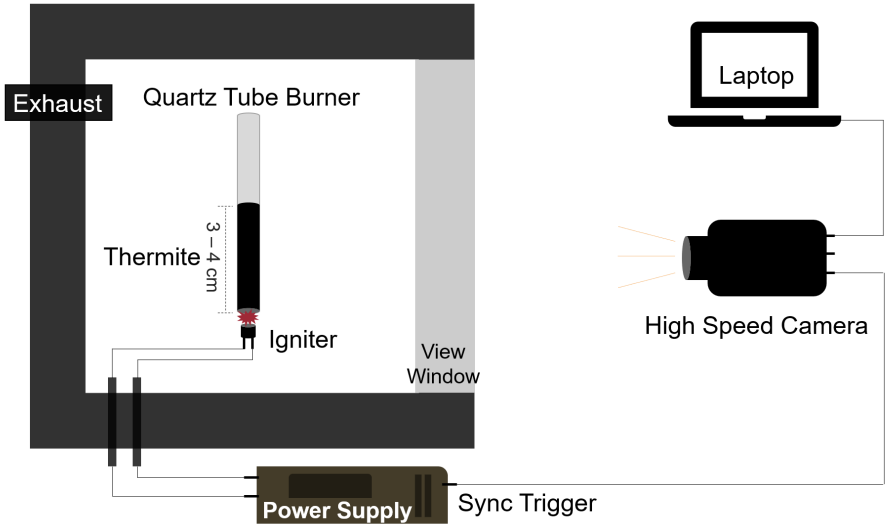

Figure 2: schematic of the combustion set-up.

camera (Phantom VEO710L-18-GB-M, USA) placed at about 1 meter away from the experimental setup, records the combustion process with a 48000-fps configuration. Three replicates of each combustion tests were conducted at ambient conditions.

5. Results and discussion

5.1. Experimental results

Figure 3 shows time-captured images of experiments conducted for the thermite samples listed in Table 3. We observe the system ignition given by the production of bright flames through a violent material ejection for all samples except for 10-µAl/CuO thermite. The detailed ignition sequence is provided in Supplementary File, Figure S1. Then, the thermite reaction propagates inside the tube delimited by the brighter section which corresponds to material vaporization. A close-up of the flame front can be found in Figure S2 of the Supplementary File. It can be observed that in the micron-sized powders, the propagation occurs irregularly with jerks due to poor compaction homogeneity as it is extremely difficult to control the compaction along the entire length of the tube. The burn rates were measured using software Phantom Camera Control and are summarized in Table 4.

The burn rate of nAl/CuO is so fast that only 5 frames were captured (Figure 3a) for the whole propagation by the high-speed camera although using the same setting as the other three samples. When the thermite particles change to micro scale, the burn rate decreases from 660 $\pm$ 75 $m.s^{-1}$ to 73 $\pm$ 15 $m.s^{-1}$ for 1-µAl/CuO indicating the significant influence of particle size on thermite propagation. Al purity and compaction are equivalent for nAl/CuO and 1µ-Al/CuO. Two possible reasons can be listed here to account for such decay: 1) larger the thermite particles slower the reaction rate because of the increased diffusion length between the fuel and oxidizer; 2) more severe sintering in microsized thermites than nanosized ones [40]. Interestingly, when the size of the Al particles reaches 10 µm (10-µAl/CuO, Figure 3d), the flame front becomes less luminous and propagates at a speed of only 10 $cm.s^{-1}$ and the flame stopped two-thirds of the way down the tube. No gas is generated during the combustion. This can be caused by a lesser content of pure Al (only 17%) in these purchased particles.

After combustion, the walls of the tube are coated with soot (see photos of post-burn tubes in Supplementary File, Figure S3) corresponding to the vaporized reaction products. Notably, in the case of the 10-µAl/CuO thermite sample, the unburned powder was pushed forward by the combustion front indicating that there is an over pressure peak in the flame front. This point will be further discussed in the upcoming section analyzing the combustion front physical properties.

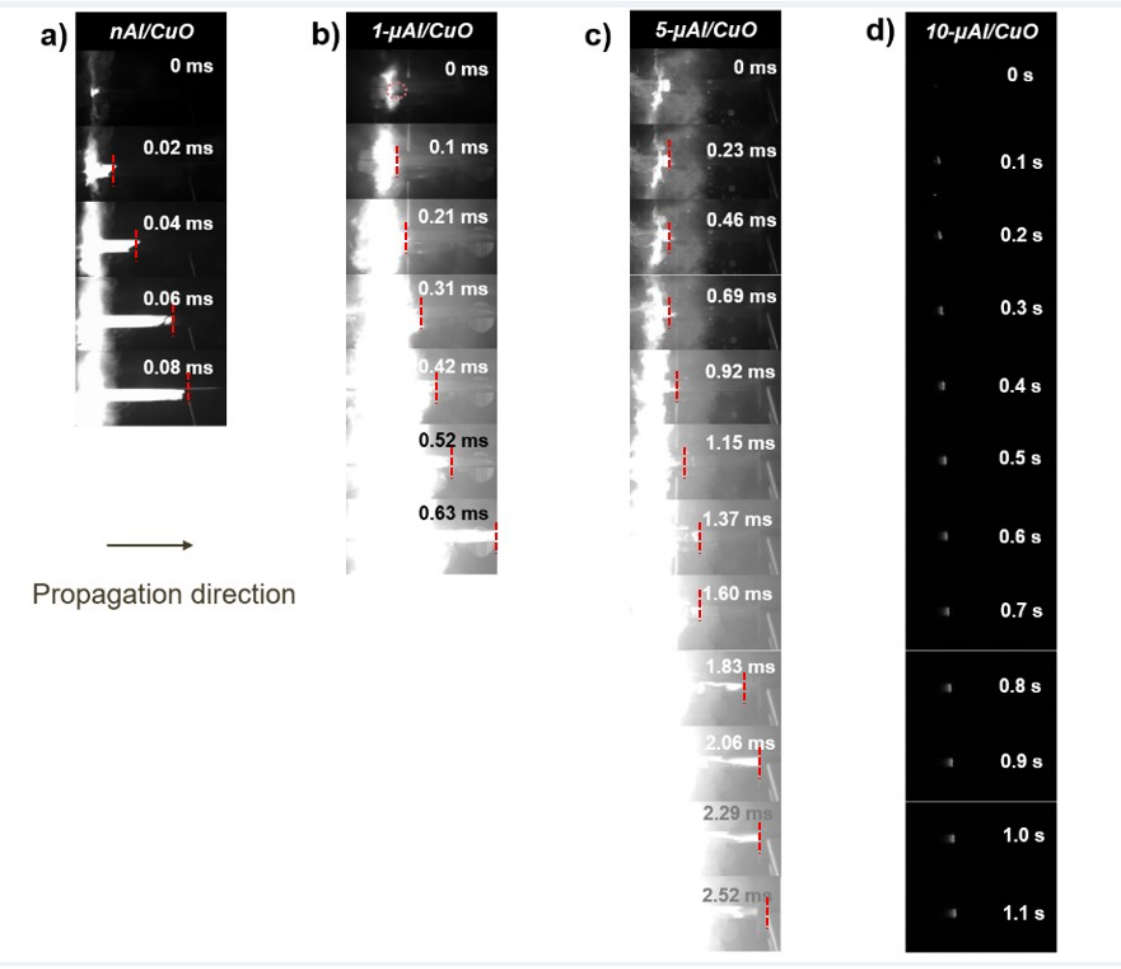

Figure 3: High-speed images of the flame propagation for nAl/CuO (a), 1-µAl/CuO (b), 5-µAl/CuO (c) and 10-µAl/CuO (d) thermite mixtures. The dashed red lines provide an approximate representation of the flame front.

5.2. Numerical results

5.2.1. Model validation

In a first experiment, we replicated the studied experimental cases to validate the model. Specifically, we used open tubes filled with thermite powders with the characteristics detailed in Table 3 in terms particles' size, powder density (α_s), Al purity and stoichiometry. Results are reported in Table 4 column 3. We see a relatively good agreement with experimental results for all thermite samples except for 10-µAl/CuO. This latter discrepancy is attributed to the fact that the 10-µAl/CuO sample fully burns in the liquid phase, as illustrated in Figure 3d, which means that no or little gas is released. As our model does not account for direct mass transfer through the particulate phase (throigh liquid particles in contact), it cannot accuratly simulate this fully-condensed phase combustion scenario. Better agreement with the results for nano-sized thermite is obtained because the overall combustion process is mostly mediated by the gas phase, which chemistry is well implemented in our model.

Table 4: Experimental burn rates *vs* theoretical burn rates

Thermites sample	**Experimental**	**Theoretical**
nAl/CuO	660 ± 75	648
1-µAl/CuO	73 ± 15	75.6
5-µAl/CuO	12 ± 5	16
10-µAl/CuO	0.01 ± 0.01	8

5.2.2. Numerical analysis of the combustion front

In a second experiment, we conducted a computational analysis of the combustion characteristics and flame propagation dynamics within glass tubes, closed at the right ends and open on the left sides. The thermite is a micron sized fuel rich and highly compacted Al/CuO thermite powder, *i.e.*, $d_p = d_q = 10$ µm, $\varphi = 1.2$, $\alpha_s = 0.5$, and Al purity is set at 80%. Figure 4 shows the thermal profile of the combustion front propagating along the tube (x-axis).

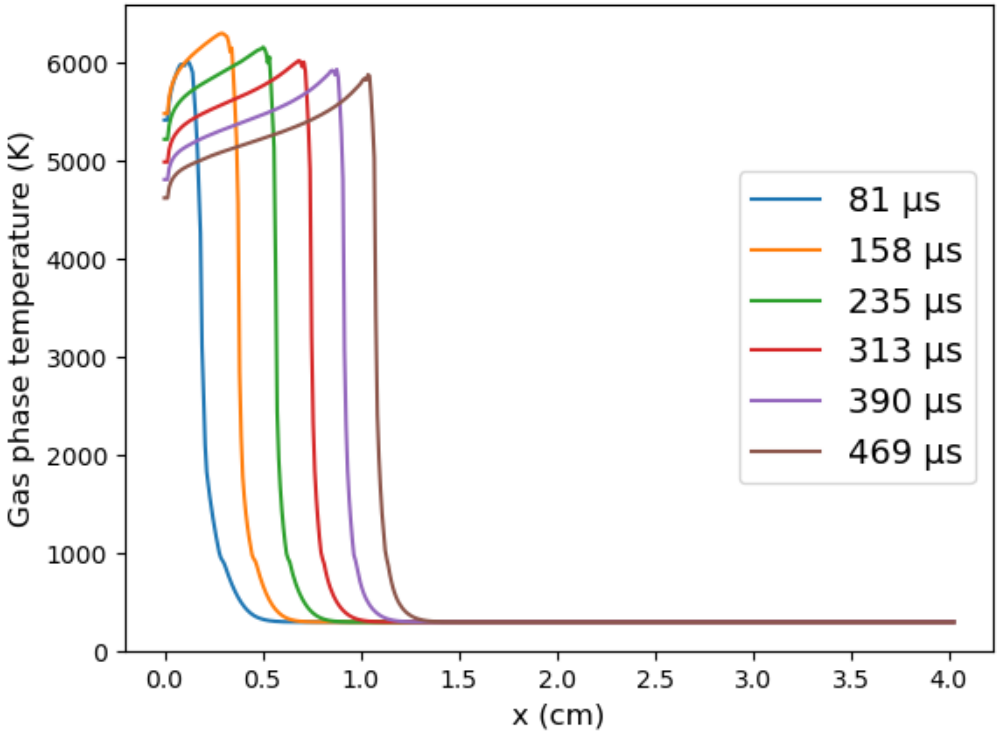

Figure 4: Snapshots of the gas temperature curves $T_g(t)$ along the tube axis at different positions x illustrating the propagation of the flame front (from left to right). The tube is opened at both ends, and reactants size = 10 µm.

The flame temperature peaks at 6000 K at the flame front, where the gas is highly compressed. It rapidly decreases upstream of the flame front in the unburnt material region (to the right side of the curves), while only slightly dropping to 4800 K downstream of the flame (to the left side of the curves).
The flame speed (u_f) establishes at around 19.7 $m.s^{-1}$, calculated as the distance covered by the flame front, 2 cm chosen between x = 0.3 cm and x = 1.3 cm, divided by the elapsed time.
Figures 5a and 5b show the volume fraction, temperature, and pressure of each phase. Figure 6 plots the composition of the gas phase downstream of the flame.

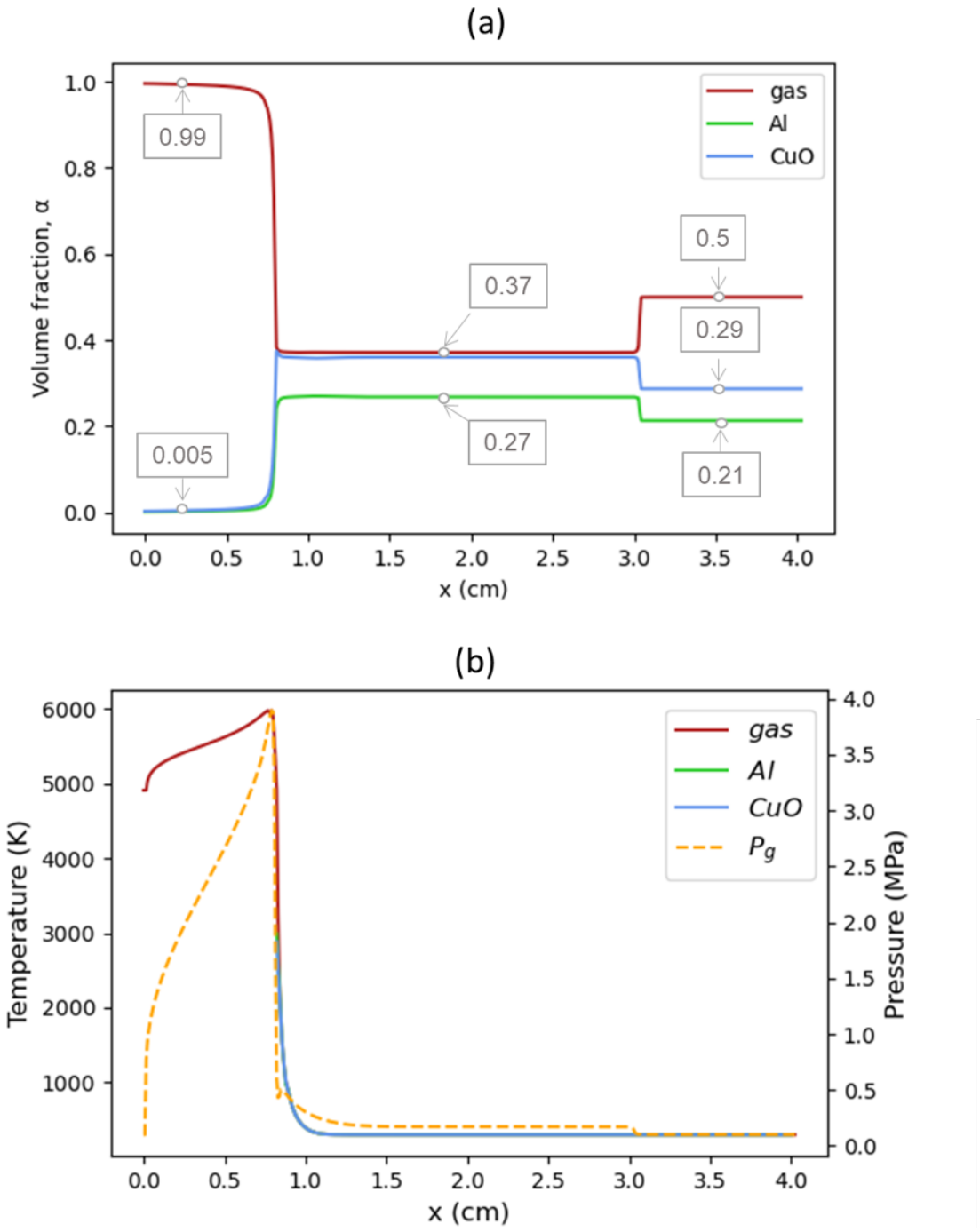

Figure 5: Spatial evolution along the tube axis of (a) the mass fraction the different phases (gas, Al and CuO), (b) the temperature of the different phases (gas, Al and CuO) and gas pressure. The tube is opened at both ends, and reactants size = 10 µm.

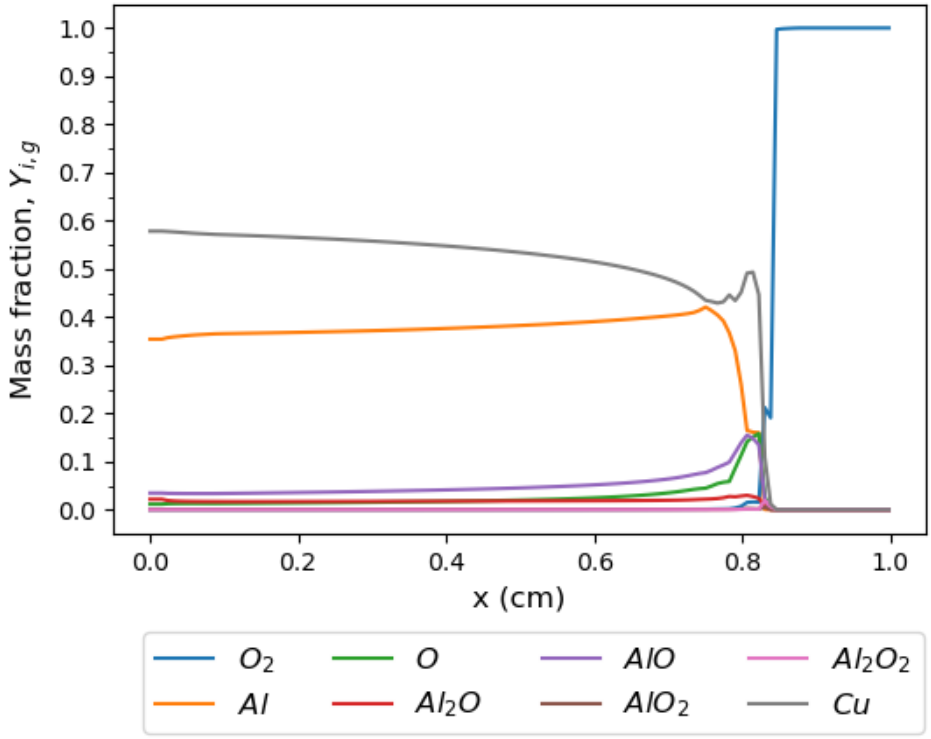

Figure 6: Spatial evolution along the tube axis of the gas phase composition. The tube is opened at both ends, and reactants size = 10 µm.

Three main regions can be distinguished along the propagation axis:
Downstream of the flame front, where combustion has occurred (*i.e.*, the 0-7.5 mm region in Figure 5): this hot region is predominantly composed of gaseous products as $\alpha_g = 0.99$, meaning that 99% of the volume is gas at temperatures exceeding 5000 K. The gas phase is mostly composed of pure copper (55%) and pure aluminum (38%) as we are in fuel rich conditions. All the oxygen was consumed to oxidize the Al. There is also some aluminum suboxides : Al_2O (2%) and AlO (4%). The remaining particle phase, which constitutes about 1% of the volume, consists of Al_2O_3 particles. We also find reduced CuO particles covered with 16% of Al_2O_3. The particles remain at high temperatures, around 3000 K, suggesting that some alumina droplets are still burning in the gas phase.
The flame zone, approximately 1.5 mm in width (between 0.75 and 0.9 cm in Figure 6), is the hottest region with the gas temperature reaching 6000 K. Interestingly, the flame front is also characterized by a pressure peak of 4 MPa associated with the maximum temperature (Figure 5b). In this region, the gas phase is mostly composed of Cu ($\sim$ 45%), O ($\sim$ 16%), AlO ($\sim$ 13%) and AlO_2 ($\sim$ 2%). This composition was recorded at one instant and one position of the flame and can vary as the flame region is not homogeneous.
Region upstream of the flame front characterized by highly packed particles, reaching a compaction of 64% ($\alpha_s = 0.64$, Figure 5a), which is the maximum possible considering spherical particles. The reaction has not yet ignited but the particles were compressed as a result of the pressure peak of 4 MPa in the flame zone. Beyond this zone, the thermite powder remains at its initial condition (compaction of 50%).

5.2.3. *Effect of powder characteristics on burn rates*

In a last numerical experiment, we study the effect of particles' size (d_p, d_q considering that $d_p = d_q$), φ, α_s, and Al purity, on the burn rates.

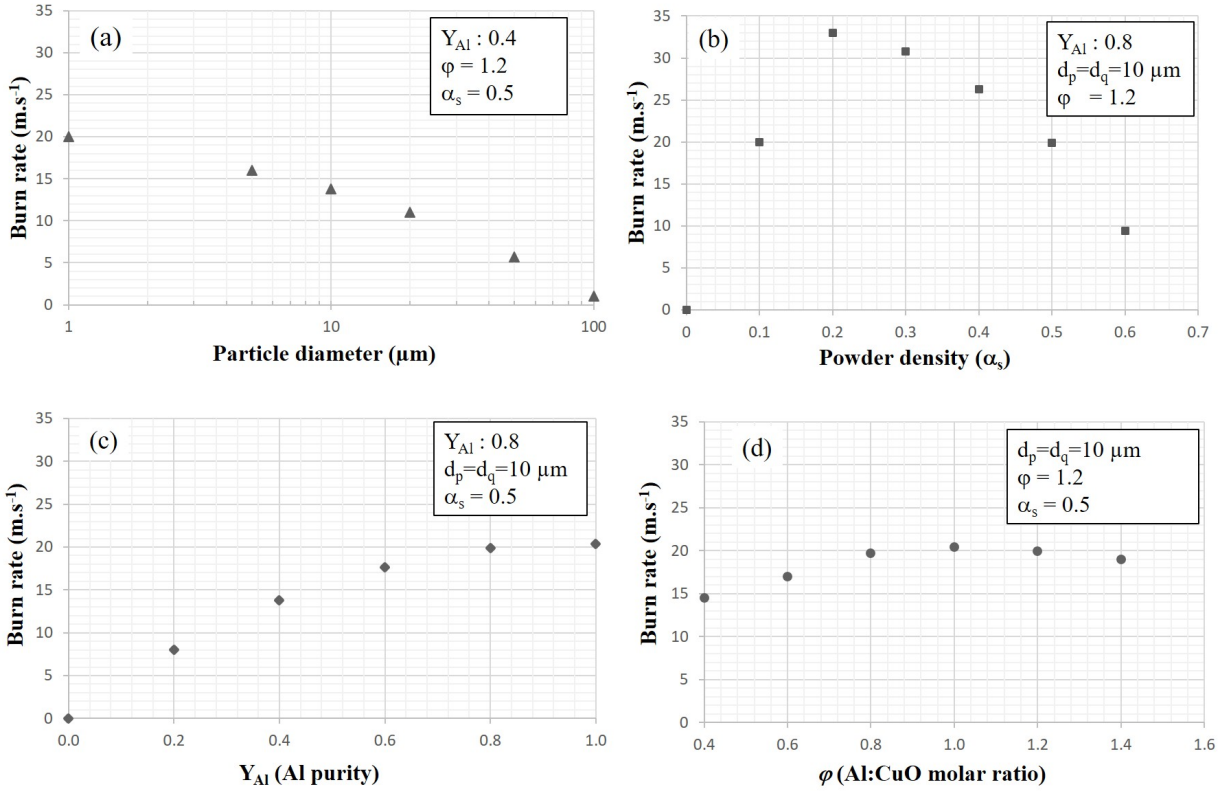

Figure 7: Impact of thermite powder characteristics on the burn rate : (a) effect of particle's size, (b) effect of α_s, (c) effect of φ, and (d) effect of Y_{Al}. The tube is opened at both ends.

The graphs in Figure 7 allow us to assess both the impact of key powder parameters on the burn rate and to explore its variability range. Particle size exerts the most significant influence on the combustion rate (Figure 7a). Specifically, within the micron to sub-micron range, the burn rate increases dramatically, by one orders of magnitude, from approximately 0.9 $m.s^{-1}$ to over 20 $m.s^{-1}$, for particles sizes decreasing from 100 µm to 1 µm respectively. Powder density is another highly influential parameter, especially in the mid-range (Figure 7b), where flame speed decreases from 33 $m.s^{-1}$ at low compaction ($\alpha_s = 0.2$) to just 10 $m.s^{-1}$ at higher compaction levels ($\alpha_s = 0.6$). Outside of these limits, flame propagation slows down and ceases. The purity of the aluminum particles also plays a significant role. For micron-sized particles, where purity can be adjusted across a wider range (Figure 7c, 10 µm Al particles), burn rates can vary from a few $cm.s^{-1}$ at low purity to up to 20 $m.s^{-1}$ with 80% pure aluminum particles. Finally, it is worth noting that stoichiometry has little effect on the burn rate when combustion occurs in ambient air (Figure 7d).

6. Conclusion

The first 1D Al/CuO thermite flame propagation model incorporating all known and documented mechanisms involved in the Al+CuO reaction has been presented. Separate mass, momentum and energy transport equations for the three phases, namely Al, CuO particles and gas phases, were implemented in the frame of an Euler-Euler approach for multiphase reactive flows. This tool has been validated through experiments on micro- and nano-scaled thermite. We demonstrated that it is accurate and well-calibrated for thermite burning in a heterogeneous regime, specifically when a large quantity of gas is produced. In that case, it enables not only an unprecedented analysis of the physics driving flame self-propagation in thermites, but also to predict average burn rate as a function of thermite parameters (reactant size, compaction rate and stoichiometry) which constitutes a notable progress in the field of thermite materials.

Acknowledgments

We thanks Ludovic Glavier from Ariane Group for the valuable scientific discussions during Emilian Tichtchenko's phD thesis and for his financial support. We extend our thank to the DGA (Direction Generale de l'Armement) and CNES (Centre National d'Etude Spatial) for funding the scholarships of Léa Pillemont and Héloïse Magliano, respectively.

References

[1] D. M. Dombroski, A. Wang, J. Z. Wen, M. Alfano, Joining and welding with a nanothermite and exothermic bonding using reactive multi-nanolayers – a review, Journal of Manufacturing Processes 75 (2022) 280–300. doi:https://doi.org/10.1016/j.jmapro.2021.12.056.
URL https://www.sciencedirect.com/science/article/pii/S1526612521009397

[2] F. J. Pena, M. J. de Lemos, Numerical investigation of an innovative through-tubing solution to thermal plug and abandonment of oil wells with thermite reactions, Applied Thermal Engineering 254 (2024) 123874. doi:https://doi.org/10.1016/j.applthermaleng.2024.123874.
URL https://www.sciencedirect.com/science/article/pii/S1359431124015424

[3] S. J. Apperson, A. V. Bezmelnitsyn, R. Thiruvengadathan, K. Gangopadhyay, S. Gangopadhyay, W. A. Balas, P. E. Anderson, S. M. Nicolich, Characterization of nanothermite material for solid-fuel microthruster applications, Journal of Propulsion and Power 25 (5) (2009) 1086–1091. arXiv:https://doi.org/10.2514/1.43206, doi:10.2514/1.43206.
URL https://doi.org/10.2514/1.43206

[4] F. Sevely, T. Wu, F. S. Ferreira de Sousa, L. Seguier, V. Brossa, S. Charlot, A. Esteve, C. Rossi, Developing a highly responsive miniaturized security device based on a printed copper ammine energetic composite, Sensors and Actuators A: Physical 346 (2022) 113838. doi:https://doi.org/10.1016/j.sna.2022.113838.
URL https://www.sciencedirect.com/science/article/pii/S0924424722004733

[5] C. S. Staley, C. J. Morris, R. Thiruvengadathan, S. J. Apperson, K. Gangopadhyay, S. Gangopadhyay, Silicon-based bridge wire microchip initiators for bismuth oxide–aluminum nanothermite, Journal of Micromechanics and Microengineering 21 (11) (2011) 115015. doi:10.1088/0960-1317/21/11/115015.
URL https://dx.doi.org/10.1088/0960-1317/21/11/115015

[6] L. Salvagnac, S. Assie-Souleille, C. Rossi, Layered Al/CuO Thin Films for Tunable Ignition and Actuations, Nanomaterials 10 (10) (2020) 2009. doi:10.3390/nano10102009.
URL https://www.mdpi.com/2079-4991/10/10/2009

[7] J.-L. Pouchairet, C. Rossi, Pyromems as future technological building blocks for advanced microenergetic systems, Micromachines 12 (2) (2021). doi:10.3390/mi12020118.
URL https://www.mdpi.com/2072-666X/12/2/118

[8] K. Kim, Computational Modeling of Combustion Wave in Nanoscale Thermite Reaction (Jan. 2018). doi:10.5281/zenodo.1093924.
URL https://doi.org/10.5281/zenodo.1093924

[9] E. Tichtchenko, A. Estève, C. Rossi, Modeling the self-propagation reaction in heterogeneous and dense media: Application to al/cuo thermite, Combustion and Flame 228 (2021) 173–183. doi:https://doi.org/10.1016/j.combustflame.2021.01.040.
URL https://www.sciencedirect.com/science/article/pii/S0010218021000584

[10] G. Lahiner, A. Nicollet, J. Zapata, L. Marín, N. Richard, M. D. Rouhani, C. Rossi, A. Estève, A diffusion–reaction scheme for modeling ignition and self-propagating reactions in al/cuo multilayered thin films, Journal of Applied Physics 122 (15) (2017) 155105. doi:10.1063/1.5000312.
URL http://aip.scitation.org/doi/10.1063/1.5000312

[11] F. J. Pena, M. J. de Lemos, Unsteady heat conduction with phase change applied to a novel thermal plug and abandonment process, International Journal of Thermal Sciences 170 (2021) 107155. doi:https://doi.org/10.1016/j.ijthermalsci.2021.107155.
URL https://www.sciencedirect.com/science/article/pii/S1290072921003173

[12] G. S. de Andrade, M. J. de Lemos, D. Colombo, A new hybrid analytical/numerical method for transient heat conduction in composite hollow cylinders applied to plug and abandonment of oil wells, International Journal of Thermal Sciences 168 (2021) 106981. doi:https://doi.org/10.1016/j.ijthermalsci.2021.106981.
URL https://www.sciencedirect.com/science/article/pii/S1290072921001472

[13] G. S. De Andrade, F. J. Pena, M. J. de Lemos, A new analytical method for transient heat conduction in composite disks applied to thermal plug and abandonment of oil wells, International Communications in Heat and Mass Transfer 155 (2024) 107465. doi:https://doi.org/10.1016/j.icheatmasstransfer.2024.107465.
URL https://www.sciencedirect.com/science/article/pii/S0735193324002276

[14] J. M. Epps, J.-P. Hickey, J. Z. Wen, Modelling reaction propagation for al/cuo nanothermite pellet combustion, Combustion and Flame 229 (2021) 111374. doi:https://doi.org/10.1016/j.combustflame.2021.02.020.
URL https://www.sciencedirect.com/science/article/pii/S0010218021000833

[15] P. Bucher, R. Yetter, F. Dryer, T. Parr, D. Hanson-Parr, E. Viceni, Flames structure measurement of single, isolated aluminum particles burning in air, Symposium (International) on Combustion 26 (2) (1996) 1899–1908. doi:https://doi.org/10.1016/S0082-0784(96)80012-9.
URL https://www.sciencedirect.com/science/article/pii/S0082078496800129

[16] L. Catoire, J.-F. Legendre, M. Giraud, Kinetic model for aluminum-sensitized ram accelerator combustion, Journal of Propulsion and Power 19 (2) (2003) 196–202. arXiv:https://doi.org/10.2514/2.6118, doi:10.2514/2.6118.
URL https://doi.org/10.2514/2.6118

[17] E. Tichtchenko, V. Folliet, O. Simonin, B. Bédat, L. Glavier, A. Esteve, C. Rossi, Combustion model for thermite materials integrating explicit and coupled treatment of condensed and gas phase kinetics, Proceedings of the Combustion Institute 39 (3) (2023) 3637–3645. doi:https://doi.org/10.1016/j.proci.2022.08.117.
URL https://www.sciencedirect.com/science/article/pii/S1540748922004588

[18] Z. Hamidouche, E. Masi, P. Fede, O. Simonin, K. Mayer, S. Penthor, Unsteady three-dimensional theoretical model and numerical simulation of a 120-kw chemical looping combustion pilot plant, Chemical Engineering Science 193 (2019) 102–119. doi:https://doi.org/10.1016/j.ces.2018.08.032.
URL https://www.sciencedirect.com/science/article/pii/S0009250918306018

[19] A. Gobin, H. Neau, O. Simonin, J.-R. Llinas, V. Reiling, J.-L. Sélo, Fluid dynamic numerical simulation of a gas phase polymerization reactor, International Journal for Numerical Methods in Fluids 43 (10-11) (2003) 1199–1220. arXiv:https://onlinelibrary.wiley.com/doi/pdf/10.1002/fld.542, doi:https://doi.org/10.1002/fld.542.
URL https://onlinelibrary.wiley.com/doi/abs/10.1002/fld.542

[20] D. Lathouwers, J. Bellan, Modeling of dense gas–solid reactive mixtures applied to biomass pyrolysis in a fluidized bed, International Journal of Multiphase Flow 27 (12) (2001) 2155–2187. doi:https://doi.org/10.1016/S0301-9322(01)00059-3.
URL https://www.sciencedirect.com/science/article/pii/S0301932201000593

[21] E. Tichtchenko, B. Bedat, O. Simonin, L. Glavier, D. Gauchard, A. Esteve, C. Rossi, Comprehending the influence of the particle size and stoichiometry on al/cuo thermite combustion in close bomb: A theoretical study, Propellants, Explosives, Pyrotechnics 48 (7) (2023) e202200334. doi:https://doi.org/10.1002/prep.202200334.
URL https://onlinelibrary.wiley.com/doi/abs/10.1002/prep.202200334

[22] P. Linstorm, Nist chemistry webbook, nist standard reference database number 69, J. Phys. Chem. Ref. Data, Monograph 9 (1998) 1–1951.

[23] P. Johnson, R. Jackson, Frictional-collisional constitutive relations for granular materials, with application to plane shearing, journal of fluid mechanics 176 (1987) 67–93. doi:10.1017/S0022112087000570.

[24] O. Simonin, S. Chevrier, F. Audard, P. Fede, Drag force modelling in dilute to dense particle-laden flows with mono-disperse or binary mixture of solid particles, in: Proc. 9th International Conference on Multiphase Flow, Firenze, Italy, 2016, pp. pp. 1–6.
URL https://hal.science/hal-01706862

[25] C. Y. Wen, Y. H. Yu, A generalized method for predicting the minimum fluidization velocity, AIChE Journal 12 (3) (1966) 610–612. arXiv:https://aiche.onlinelibrary.wiley.com/doi/pdf/10.1002/aic.690120343, doi:https://doi.org/10.1002/aic.690120343.
URL https://aiche.onlinelibrary.wiley.com/doi/abs/10.1002/aic.690120343

[26] S. Ergun, A. A. Orning, Fluid flow through randomly packed columns and fluidized beds, Industrial & Engineering Chemistry 41 (6) (1949) 1179–1184. arXiv:https://doi.org/10.1021/ie50474a011, doi:10.1021/ie50474a011.
URL https://doi.org/10.1021/ie50474a011

[27] D. Gunn, Transfer of heat or mass to particles in fixed and fluidised beds, International Journal of Heat and Mass Transfer 21 (4) (1978) 467–476. doi:https://doi.org/10.1016/0017-9310(78)90080-7.
URL https://www.sciencedirect.com/science/article/pii/0017931078900807

[28] S. S. Sih, J. W. Barlow, The prediction of the emissivity and thermal conductivity of powder beds, Particulate Science and Technology 22 (3) (2004) 291–304. arXiv:https://doi.org/10.1080/02726350490501682a, doi:10.1080/02726350490501682a.
URL https://doi.org/10.1080/02726350490501682a

[29] M. N. Ozisik, Heat transfer: a basic approach, Vol. 1, McGraw-Hill New York, 1985.

[30] O. Simonin, Statistical and Continuum Modelling of Turbulent Reactive Particulate Flows. Part 1: Theoretical Derivation of Dispersed Eulerian Modelling from Probability Density Function Kinetic Equation, Rhode Saint Genèse, Belgium, 2000.

[31] M. Chase, NIST-JANAF Thermochemical Tables, 4th Edition, American Institute of Physics, -1, 1998.

[32] D. G. Goodwin, R. L. Speth, H. K. Moffat, B. W. Weber, Cantera: An Object-oriented Software Toolkit for Chemical Kinetics, Thermodynamics, and Transport ProcessesVersion 2.5.1 (2021).

[33] R. A. Svehla, Estimated viscosities and thermal conductivities of gases at high temperatures, 1962.
URL https://api.semanticscholar.org/CorpusID:96366158

[34] S. Gallier, F. Sibe, O. Orlandi, Combustion response of an aluminum droplet burning in air, Proceedings of the Combustion Institute 33 (2) (2011) 1949–1956. doi:https://doi.org/10.1016/j.proci.2010.05.046.
URL https://www.sciencedirect.com/science/article/pii/S1540748910001124

[35] V. Baijot, D.-R. Mehdi, C. Rossi, A. Estève, A multi-phase micro-kinetic model for simulating aluminum based thermite reactions, Combustion and Flame 180 (2017) 10–19. doi:https://doi.org/10.1016/j.combustflame.2017.02.031.
URL https://www.sciencedirect.com/science/article/pii/S0010218017300780

[36] M. L. Narula, V. B. Tare, W. L. Worrell, Diffusivity and solubility of oxygen in solid copper using potentiostatic and potentiometric techniques, Metallurgical Transactions B 14 (4) (1983) 673–677. doi:10.1007/BF02653953.
URL https://doi.org/10.1007/BF02653953

[37] A. Vorozhtsov, M. Lerner, N. Rodkevich, H. Nie, A. Abraham, M. Schoenitz, E. Dreizin, Oxidation of nano-sized aluminum powders, Thermochimica Acta 636 (2016) 48–56. doi:https://doi.org/10.1016/j.tca.2016.05.003.
URL https://www.sciencedirect.com/science/article/pii/S0040603116301125

[38] M.-S. Liou, A sequel to ausm, part ii: Ausm+-up for all speeds, Journal of Computational Physics 214 (1) (2006) 137–170. doi:https://doi.org/10.1016/j.jcp.2005.09.020.
URL https://www.sciencedirect.com/science/article/pii/S0021999105004274

[39] T. Wu, V. Singh, B. Julien, M.-I. Mendoza-Diaz, F. Mesnilgrente, S. Charlot, C. Rossi, Design and fabrication of a fast-response and low-energy input micro igniter, Sensors and Actuators A: Physical 376 (2024) 115573. doi:https://doi.org/10.1016/j.sna.2024.115573.
URL https://www.sciencedirect.com/science/article/pii/S0924424724005673

[40] K. Sullivan, N. Piekiel, C. Wu, S. Chowdhury, S. Kelly, T. Hufnagel, K. Fezzaa, M. Zachariah, Reactive sintering: An important component in the combustion of nanocomposite thermites, Combustion and Flame 159 (1) (2012) 2–15.

doi:https://doi.org/10.1016/j.combustflame.2011.07.015.
URL https://www.sciencedirect.com/science/article/pii/S0010218011002276